Porous Electrodepositions Influence on Conical Flames Stability in Unconfined Single-point Injection Burners

André Henriques Marques Neves
andre.henriques.neves@ist.utl.pt

Instituto Superior Técnico, Universidade de Lisboa, Portugal

November 2018

Abstract

With a future purpose to expand the analysis to multiperforated plate burners, the present work evaluates the flame stability influence of specific surface manipulations of the anchoring plate's perforation inner wall in an unconfined single-perforated plate burner.

Using the dynamic hydrogen bubble template (DHBT) method, four 3D porous electrodepositions were performed in upward chamfered plates. Samples A and B were considered coatings, thin layers covering the plate's chamfer, while Samples C and D were termed fillings, large foams reconstructing the plate's chamfer. Sample A was mainly composed by cobalt (Co), presenting a honeycomb-like structure, but Samples B, C and D were essentially composed by a zinc (Zn)-derived (simonkolleite), presenting a morphology embodied by hexagon-like sub-units. Sample D was the only one presenting pore interconnectivity.

For the thickness intervals characteristic of industrial applications of electrodepositions, flame stability in an upward chamfered plate isn't relevantly affected by the chamfer's coating thermal conductivity (λ) or its variation during operation ($\frac{\partial \lambda}{\partial T}$).

A porous reconstruction of an upward chamfered plate's chamfer, which restricts the incoming reactant flow crossing area at the plate's bottom, might affect the flame's dynamics to a point where, for a particular unstable operating condition, its former coupling with the (unaltered) burner's acoustics is disrupted.

A porous reconstruction of an upward chamfered plate's chamfer, with a high pore interconnectivity level and an appropriately tuned pore size, mitigates the flame's ability to develop self-sustained thermoacoustic instabilities, apparently by increasing the local thermoviscous effects and consequently enhancing the burner's acoustic damping.

Keywords: Flame stability, thermoacoustic instabilities, 3D porous electrodepositions, single-perforated plate

1. Introduction

In 2016 more than 90% of the world's energy production came from fossil fuels, biofuels and waste. To enable its final consumption, their chemical energy must be converted into thermal energy (mainly) by the process of combustion. This reaction's strong exothermic behaviour is precisely what guarantees its critical role in global energy production, but also invites its employment in several other areas like the thermotechnology industry. Nonetheless, the combustion of the aforementioned hydrocarbon fuels presents grave environmental and health implications due to the pollutant and toxic character of some of its products, specifically nitrogen oxides (NO_X) and carbon monoxide (CO). To enable a reduction of these pollutants emissions, the heating industry changed the way open flame burners are designed, giving rise to multiperforated burners, whose application nowadays varies from industrial dryers to domestic boilers. However, the low flame temperature conditions in which these burners are operated and the strong flame-flame interactions inherent to their design make them increasingly more prone to the occurrence of thermoacoustic instabilities than a single-perforation configuration [1, 2].

This phenomenon has been known for around 150 years, such that thermoacoustic instabilities can be interpreted as unsteady high-speed variations of the flame's heat release based on a flame-burner acoustic coupling, governed by the flame's dynamics and the burner's acoustic characteristics.

Historically, these oscillations were corrected by trial-and-error design of the burner, but due to a growing need to operate in very large modulation ranges this method has become non-viable. Hence,

an accurate acoustic modelling of the system has become a critical part of its design phase. An extensive research has been performed on open flame burners with several configurations, from which a few studies can be denoted. [3] exposed the importance of flame-wall interactions as a driving mechanism for self-induced thermoacoustic instabilities. [2] established the role of mutual flame interactions as a driving mechanism for self-sustained thermoacoustic instabilities. Later, [4] attempted a greater approximation to burner geometries used in industrial process applications, studying the development of self-sustained thermoacoustic instabilities on premixed conical laminar flames anchored on a multiperforated plate (MPP) burner. Continuing this investigation, [5] presented passive control solutions to suppress combustion-driven instabilities by increasing the plate's thickness and controlling the perforations' diameter. More recently, [6] introduced the importance of the plate's perforation ratio in the development of self-sustained thermoacoustic instabilities on an MPP burner.

Besides this, the literature still presents several ways flame stability can be improved in an industrial scenario. From existing reviews, some authors can be recognized such as [7] and [8] for their work in confined burner configurations or [5] for his studies in unconfined ones. As presented by [7], active control solutions intend to condition the system's stability based on a time-varying adjustment, relying on control systems whose operation depends on a dynamic hardware component (actuator). Passive control solutions on the other hand change flame stability trough time-fixed modifications, without resorting to any actuators [7]. Existing approaches typically attempt to avoid a coincidence between the burner's frequency bandwidth and the flame's unstable frequency ranges, disabling the flame-burner acoustic coupling. This can be achieved by changes to the burner's acoustics or to the the flame's convective time delay.

In conclusion, despite the significant potential of active control methods, they encompass several practical problems which have lead the heating industry to focus primarily on passive control techniques whose simplicity facilitates its commercial applicability [5].

The objective of the present work is to provide a basis for the creation of a simple and flexible passive method to minimize the development of self-sustained thermoacoustic instabilities in modern open flame MPP burners. To maximize the obtained solution's application limits, the mitigation of the flames' unstable behaviour should be achieved by enabling an increase of the system's acoustic damping and not by avoiding an overlap between the burner's frequency bandwidth and the flame's unstable frequency ranges. Since the burner's acoustic resistance is essentially determined by the thermoviscous effects in the perforations' inner wall boundary layer [5], the present study focuses on manipulating such wall surface conditions by applying different depositions and analysing the influence of those depositions on flame stability.

2. Experimental setup

The flame's stability was examined in an unconfined single-point injection configuration, where a premixed air-propane conical laminar flame is anchored on a single-perforation plate. Burner configuration is presented in Figure 1 and was inspired by the one used by [4, 5].

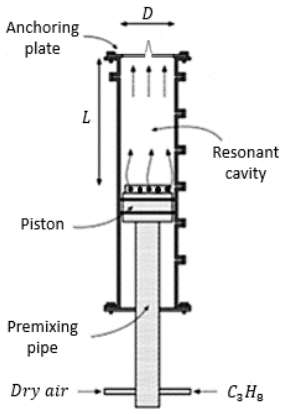

Figure 1: Schematic depiction of the burner apparatus used.

The system is essentially comprised by a premixing pipe, a resonant cavity and a single-perforation plate. The reactant mixture is injected into a "V" shape connection at the lower part of the premixing pipe, where it flows up to the resonant cavity and is fed to it through twelve apertures around the piston's head, which presents a 42 mm diameter. The resonant duct presents a 43,5 mm internal diameter (D) and a variable length (L) defined the piston's head position, allowing to control the burner's acoustic behaviour. It is enclosed at its bottom by the piston's flat head, establishing a quasi-perfect acoustical reflection boundary, and at its top by the single-perforation plate, where the conical flame anchors. This forms an unconfined reaction zone which reproduces to some extent the conditions found in some modern heating devices [5]. The annular gap between the piston and the resonant duct is sealed with an O-ring made of polytetrafluoroethylene (PTFE). The geometrical characteristics of the system's resonant cavity are exposed in Table 1.

The system's stability is conditioned by the flame's dynamics and the burner's acoustics.

Table 1: Geometrical dimensions of the burner's resonant cavity.

Resonant duct	mm
Length L	10< L <700
Internal diameter D	43.5

The former is determined by the reactant flow's Reynolds number (Re) and equivalence ratio (ϕ), while the latter is controlled by the resonant cavity length L, whose variation translates in a shift of the burner's frequency bandwidth when exposed to an external excitation, emulating the acoustics of a variety of commercial burners. The fuel used was propane (C_3H_8) and the oxidizer was atmospheric dry air ($dry\,air$), filtered using a water filter. The stability tests were performed using an experimental setup schematically depicted in Figure 2. Two precision gas flow meters (Alicat Scientific, MC series) with maximum capacities of 5 and 1 standard litters per meter (SLPM) were used to control the air and propane flow rates, respectively, using the Flow Vision^{TM} software with an user interface developed in LabVIEW.

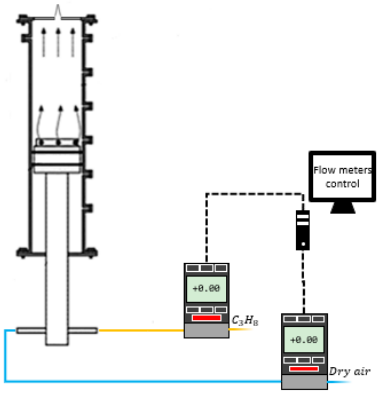

Figure 2: Schematic representation of the experimental setup used for flame stability analysis.

For a defined resonant duct length L, tests were conducted at constant equivalence ratios sweeps: for each ϕ, the mixture's Re was lowered from blowoff conditions to (or near) flashback, starting at rich values and then decreasing ϕ to leaner regimes. For each point of interest, an average of at least three measurements was performed and flame instability was recognized trough flame visualization and hearing. The maximum thermal power yielded in the operated conditions was 3.7 kW. Four single-perforation plates were tested, presented in Figure 3. According to their perforation, they can be divided into straight edge perforation plates (SE plate) or upward chamfered plates (Benchmark plate and plates I and II). All plates are made of stainless steel (SS) with a 2 mm thickness (l) and

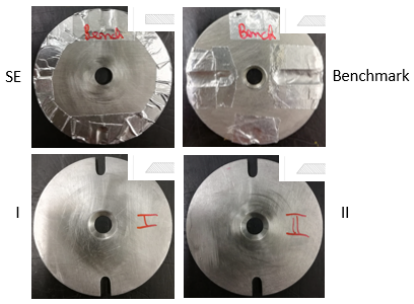

Figure 3: Single-perforation flame-anchoring plates. SE: straight edge plate; Benchmark: Benchmark plate; I: Plate I; II: Plate II. All plates present a chamfered perforation, except for the SE plate which presents a straight perforation.

a perforation with a 6 mm bottom diameter. However, while the SE plate presents a straight perforation, with equal bottom and top diameter, the other plates present a (roughly) 45° upward chamfer, with a 6 mm bottom diameter d and a 10 mm top diameter (t). Plates I and II were the ones used to test the depositions. The full geometrical parameters of each plate may be checked in Table 2.

Table 2: Geometrical dimensions of the flame-anchoring plates (in mm).

Single-perforation plate	**SE**	**Benchmark**	**I**	**II**
Thickness l	2			
Perforation bottom diameter d	6			
Perforation top diameter t	6	10		

Using plates I and II, a total of four chamfer deposition samples were tested in this work. Depending on their architecture, they were identified as coatings (Samples A and B) – thin layers covering the plate's chamfer - or fillings (Samples C and D) – large deposits on the plate's chamfer aimed at reconstructing and "straighten" it, making its top diameter identical to the bottom one (d = 6 mm). To perform them, two precursor electrolyte solutions were prepared: one to deposit a zinc (Zn)-derived – containing 0.5 M $ZnCl_2$ (Sigma-Aldrich) and 2 M NH_4Cl (Roth) – and another to deposit cobalt (Co) – containing 0.1 M $CoCl_2.6H_2O$ (Roth), 1.5 M NH_4Cl (Roth) and 0.5 M NaCl (Sigma-Aldrich). Both solutions were prepared from analytical grade chemicals and distilled water. Previous to the electrodeposition, the plate to be deposited was cleaned with acetone in ultrasound and dried with a jet of cold air. All electrodepositions were conducted employing the dynamic hydrogen bubble template (DHBT) method at room temperature in an electrolytic cell, using a Kikusui Electronics power source (Model PAB 32-3). A graphite plate was used as a counter electrode, while the plate to be deposited was used as a working elec-

trode, presenting an active surface area of 0.71 cm^2 (equal to its chamfer area). Depending on the deposition sample, the procedure was carried out on a galvanostatic mode (constant current) or on a pulsed mode (pulsed current), for a defined exposure time. Each sample's electrodeposition parameters are summarized in Table 3. After this procedure, the deposited plate was rinsed in distilled water and left to dry for a day.

Table 3: Electrodeposition parameters used to synthesize each sample. Samples A, B and D were performed with constant current, while Sample C was obtained with pulsed current (30 s intervals).

Electrodeposition sample	Electrolyte composition	Current density i (A/cm^2)	Exposure time t_{exp} (s)
Sample A	0.1 M $CoCl_2.6H_2O$ + 1.5 M NH_4Cl + 0.5 M NaCl	0.37	180
Sample B	0.5 M $ZnCl_2$ + 2 M NH_4Cl	0.23	90
Sample C	0.5 M $ZnCl_2$ + 2 M NH_4Cl	3.45	420 (30s pulses)
Sample D	0.5 M $ZnCl_2$ + 2 M NH_4Cl	2.69	240

Given the high level growth of metallic deposits required to obtain the synthesized fillings (Samples C and D), during these samples electrodeposition procedures, a cylindrical pin was placed inside the corresponding chamfered plate's perforation to provide interior support for the growing metal deposit and delimit its inner wall geometry and dimensions. The cylindrical pin presented a 5 mm length and a 5.5 mm diameter, so that when covered with electrical tape would practically present a diameter equal to d.

The crystal structures of the synthesized deposition samples were investigated using X-ray diffraction (XRD). Diffractograms were recorded at room temperature by a Bruker AXS-D8 Advance powder diffractometer with a Bragg-Brentano geometry [Cu Kα radiation source ($\lambda_{wave} = 0.150619\,nm$)] and the diffraction patterns were collected over a 2θ range of incidence angles from 10° to 90°, with a 0.02° step size. The morphological characterization of these samples was performed using Scanning Electron Microscopy (SEM, Hitachi S2400) and the elemental chemical analyses were performed by its corresponding Energy Dispersive Spectrometer (EDS).

3. Results

3.1. Deposition samples characterization

From the four deposition samples tested in this investigation, two different compositions emerged: one in Sample A and another in Samples B, C and D.

Figure 4 shows the X-ray diffractogram of Sample A, presenting the intensity of its diffracted X-ray beams as a function of the incidence angle 2θ. According to [9], the diffraction peaks at the incidence angles of 44.4° and 76.2°, signalled by plus signals, can be respectively indexed to the (111) and (220) crystal planes of face-centered cubic Co, while the ones at 41.8° and 47.3°, also signalled by plus signals, can be respectively associated to the (100) and (101) crystal planes of hexagonal close-packed Co. This indicates the presence of Co arrays in the performed deposition. The relative sharpness of such diffraction peaks reflects the high crystallinity of the deposited Co. Moreover, the EDS analysis of this sample revealed the presence of Co (75.2 norm. at. %[1]), oxygen (O) (15 norm. at. %) and carbon (C) (9.8 norm. at. %), confirming the presented XRD results.

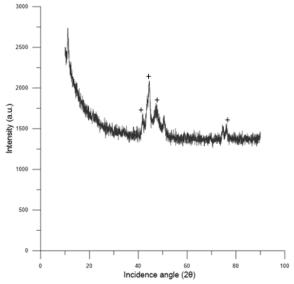

Figure 4: XRD pattern of Sample A.

Figure 5 presents the X-ray diffractogram of Samples B, C and D. The sharp intensity peaks indexed by an asterisk, particularly at the incidence angles of 11.3°, 28.3°, 32.9°, 36.2° and 58.3°, are characteristic of the cristal planes of hexagonal close-packed $Zn_5(OH)_6(Cl)_2.H_2O$ (simonkolleite) (RRUFF ID: R130117), indicating the presence of simonkolleite arrays with high crystalline purity in the performed depositions [10]. Furthermore, the EDS analysis of these samples revealed the presence of Zn (48.4 norm. at. %), O (39.7 norm. at. %) and chloride (Cl) (11.9 norm. at. %), supporting the shown XRD results.

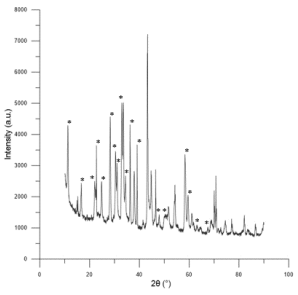

Figure 5: XRD pattern of Samples B, C and D.

The synthesized samples morphology can be visualized in Figure 6, where a 3D porous structure, typical of foams constructed by DHBT, is common to all cases. Nonetheless, there are still clear mor-

[1]The normalized atomic percentage (norm. at. %) represents the percentage of the total amount of atoms of a given substance out of the total number of atoms of every substance present in the studied sample.

phological differences between samples consequent of the electrodeposition parameters used for each: while Sample A presents a honeycomb-like structure with relative homogeneity, as depicted by [11], Samples B, C and D present a morphology composed by hexagon-like sub-units, typical of simonkolleite, as described by [10]. Also, while Sample D presents an interconnected network of pore walls, the other Zn-derived samples do not.

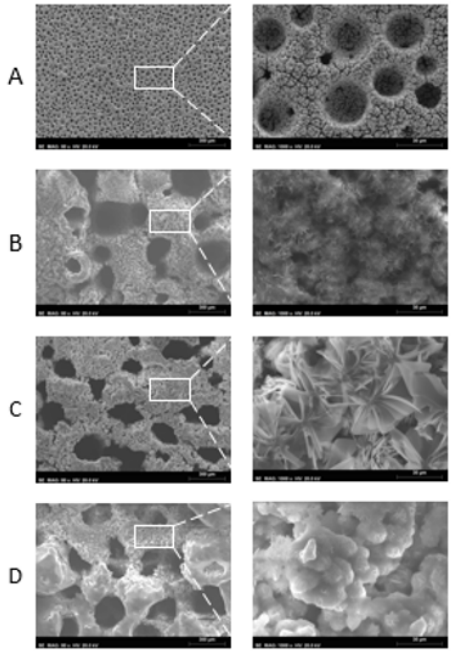

Figure 6: SEM micrographs showing top-down views of the synthesized samples. The images on the left correspond to a 80X amplification of the corresponding sample, while the images on the right correspond to a 1000X amplification of the area delimited in white.

Given its particular architecture, the synthesized fillings (Samples C and D) ability to reconstruct the corresponding plate's chamfer, using the interior support pin in the process, and "straighten" it, making the perforation's top diameter equal to its bottom, was evaluated. Using the Image J software, the samples' top diameter was calculated and compared to the plate's bottom diameter d. Results are presented in Table 4. As it shows, although both samples were not able to fully "straighten" the plate's chamfer perforation, Sample D performed a more complete chamfer reconstruction than Sample C.

Table 4: Geometrical dimensions of synthesized fillings (Samples C and D).

Filling	Perforation bottom diameter d (mm)	Reconstructed perforation top diameter (mm)	Reconstruction proximity (%)
Sample C	6	7.85	69.17
Sample D	6	6.67	88.83

3.2. Flame stability analysis

With a long-term view to mitigate self-sustained thermoacoustic instabilities in modern open flame MPP burners, flame stability diagrams (FSDs) under several experimental conditions (L, anchoring plate, deposition sample) were obtained for the unconfined single-point injection configuration described. These maps are here presented and a thorough physical interpretation of their results is performed.

SE plate vs Benchmark plate

Considering the choice of using anchoring plates with an upward chamfered perforation to analyse the presented depositions influence on flame stability, instead of the more industrially present straight edge perforation design, it was important to first evaluate this perforation's geometry influence on the system's stability.

To do so, FSDs were measured for the burner using a straight edge perforation plate, SE plate, and an upward chamfered plate, Benchmark plate, for three different resonant cavity lengths, $L \in \{10.5, 20, 35\}$ (cm). Both plates' results were then compared with one another for every resonant cavity size in Figure 7.

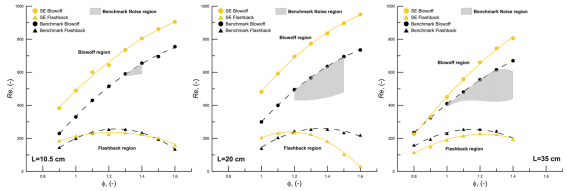

Figure 7: Overlap of the flame stability maps of the SE plate and the Benchmark plate for several resonant duct lengths. The map on the left was obtained for $L = 10.5$ cm, the map on the center was obtained for $L = 20$ cm and the map on the right was obtained for $L = 35$ cm. The SE plate is associated to yellow symbols while the Benchmark plate is associated to black symbols. The shaded area corresponds to Benchmark plate's self-sustained unstable combustion region.

For the considered equivalence ratios, the SE plate presents a higher flame stability than the Benchmark plate and while the former one does not induce self-sustained thermoacoustic instabilities, the latter one does. Besides this, although the SE plate's stability region is independent of the resonant duct length, the Benchmark plate's blowoff limit exhibits a slight variation with it, which becomes more noticeable for leaner ϕ. Finally, the Benchmark plate's instability region size varies with the burner's resonant cavity length.

Considering both plates present an identical perforation bottom diameter d and a small thickness l, the fresh reactant flow velocity profile at the plate's outlet is assumed equal in both cases; hence, the

system with the highest laminar flame speed S_L should be the most stable one. According to [12], for rich conditions ($\phi > 1$), the entrainment of the surrounding atmospheric air at the flame's base results in a dilution of the burning mixture, which approximates its equivalence ratio to stoichiometric conditions ($\phi \sim 1$). This will increase the flame's local burning temperature and consequently the local S_L. For lean conditions ($\phi < 1$), the opposite occurs and the mixture's dilution due to exterior air entrainment at the flame's base will move its equivalence ratio away from stoichiometric conditions, decreasing the S_L in that area.

For the entire operating conditions analysed, the Benchmark plate's flame is always inside its chamfer. There, due to the positive pressure induced by the upstream premixture flow, it is considered to be much less exposed to dilution from the surrounding air than the SE plate's flame. Thus, considering the results obtained by [12], while rich flames should be more stable in the SE plate, lean flames should be more stable in the Benchmark plate.

The results represented in Figure 7, somewhat translate this, particularly those for $L = 35$ cm where both rich and lean regimes were considered ($\phi \in [0.8, 1.4]$). In the latter, a crossing between the plates' blowoff lines occurs near $\phi = 0.85$, such that the SE plate is more stable for $\phi > 0.85$ and the Benchmark plate is more stable for $\phi < 0.85$.

Benchmark plate = function(L)

Considering the Benchmark plate's instability region variation with L depicted in Figure 7, a deeper characterization of its stability behaviour was required. Thus, its FSDs were acquired for a wider range of cavity sizes ($L \in [5, 40]$ (cm)) and compared with each other in Figure 8.

Although the flame's stability limits are fairly identical for all resonant duct lengths, there is a clear non-linear dependence between the size and location of the upward chamfered plate's acoustically unstable region and L. For the tested cavity sizes, such noise area is largest for $L \in \{20, 30, 35\}$ (cm) and smallest for $L \in \{5, 40\}$ (cm), qualitatively presenting, trough hearing, its highest sound pressure level (SPL) at $L = 35$ cm.

This non-linear behaviour is in agreement with the findings presented by [4] that, for a defined flame (constant Re and ϕ), conditions associated to acoustic instabilities alternate with ones characterized by stable combustion for a growing resonant cavity.

To properly evaluate the performed depositions influence on flame stability, the worst-case scenario was selected, studying such influence at the resonant cavity condition for which the Benchmark plate instability region was considerably large and its associated SPL was the highest, $L = 35$ cm.

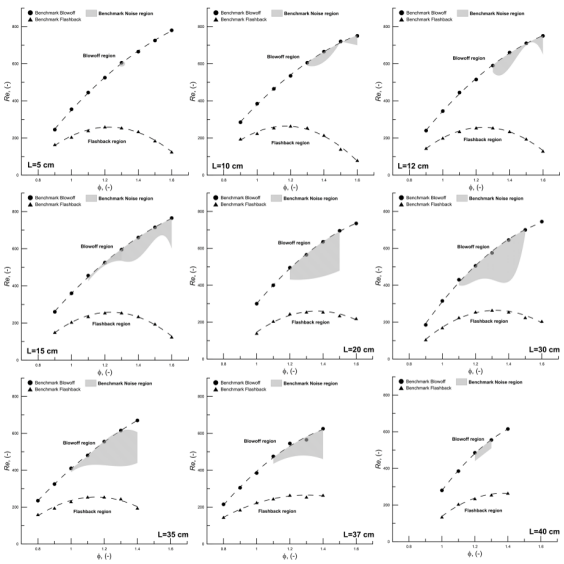

Figure 8: Flame stability maps of the Benchmark plate for a wide range of resonant duct lengths, $L \in \{5, 10, 12, 15, 20, 30, 35, 37, 40\}$ (cm). The shaded area corresponds to Benchmark plate's self-sustained unstable combustion region.

Plate I vs plate II

Having understood the influence of a chamfer perforation design and identified the resonant duct length at which combustion instabilities are more severe in the tested burner apparatus, a characterization of the upward chamfered plates effectively used to evaluate the performed depositions influence on flame stability (plates I and II) was imperative.

To do so, its FSDs were obtained for the defined resonant duct length ($L = 35$ cm) and compared with each other in Figure 9.

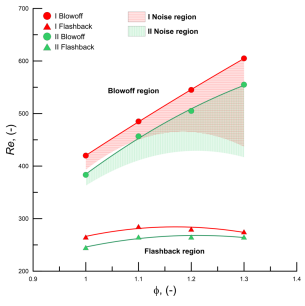

Figure 9: Overlap between plates I and II stability maps for $L = 35$ cm. Plate I is associated to red symbols while plate II is associated to green symbols. The red and green shaded areas correspond to plates' I and II self-sustained unstable combustion regions, respectively.

Albeit the plates were manufactured with the same techniques to present identical geometries

and dimensions, they show different stability behaviours, with some variations around the position of their flammability limits and their respective noise regions. Nonetheless, such limits and noise regions maintain the same shape across both plates, presenting only an offset between them and thus suggesting that those differences are linear.

Such offset may be due to the fact that the plates chamfers were manually performed, which possibly has led to slightly different chamfer geometries that may have changed the flame-plate heat balance for each anchoring plate.

To prevent these differences from introducing errors in the present work's conclusions, plates I and II were treated as individually unique, such that the performed depositions influence on flame stability can only be evaluated by comparing the deposited plate's behaviour with the same plate's behaviour in the absence of electrodepositions.

Addressing the present work's short-term objective to evaluate the characterized chamfer depositions influence on flame stability, a set of deposition case-studies is here presented. The performed analyses establish variations regarding: the thermal behaviour of the deposited material, the architecture of its macrostructure and the morphology of its microstructure.

Co coating vs Zn-derived coating

The first case-study intended to analyse the impact of the anchoring plate's chamfer thermal conductivity (λ) and its variation during operation ($\frac{\partial \lambda}{\partial T}$) in the flame's stability. To achieve this, plates' II and I chamfers were coated with Samples A and B, respectively. As described in Section 3.1, Sample A was essentially composed by Co, a material whose thermal conductivity is 105 W/(m*K) at NTP conditions [13] but which decreases with temperature ($\frac{\partial \lambda}{\partial T} < 0$), acting as an insulating coating for the chamfer's surface. Sample B on the other hand was mainly composed by a Zn-derived (simonkolleite), a material whose thermal conductivity is 117 W/(m*K) at NTP conditions [13] but which increases with temperature ($\frac{\partial \lambda}{\partial T} > 0$), acting as a conductive coating for the chamfer's surface. To minimize the coatings' effect on the incoming flow's velocity profile at the plate's outlet, both samples' electrodeposition parameters were tuned to minimize their thickness and ensure a porous morphology.

Following this, the deposited plates' FSDs were acquired for the defined resonant duct length and compared to their respective behaviour in the absence of electrodepositions. Results are presented in Figure 10.

For both chamfer-coated plates, flame stability does not appear to be relevantly affected by the deposition's presence, presenting a blowoff limit identical to the one in non-deposited conditions and an instability region whose size and location is also reasonably similar to the one in clean conditions.

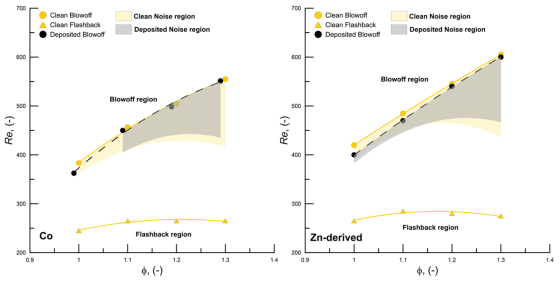

Figure 10: Overlap of plates' II and I stability maps in coated and non-coated conditions for $L = 35$ cm. The map on the left analyses the Co coating of plate II while the map on the right studies the Zn-derived coating of plate I. The non-deposited plate is associated to yellow symbols while the deposited plate is associated to black symbols. The yellow and grey shaded areas correspond to the non-deposited and deposited plates' self-sustained unstable combustion regions, respectively.

This may suggest that the plate's chamfer thermal conductivity λ does not significantly alter the flame-plate heat balance, hinting that the chamfer surface does not have a relevant role in flame stabilization. Nonetheless, considering the results presented in Figure 9 and theory on the stabilization mechanism of premixed flames, it is considered more likely that both coatings present such a small thickness that their impact on the chamfer's global conductive behaviour is negligible, making it perform identically regardless of the coatings presence.

As described by [14], the phenomenon of acoustic dissipation by means of a solid structure consists on the conversion of said acoustic energy into two main forms of energy: thermal energy, due to the viscous effects experienced inside the flowing medium and between it and the structure's surface, and strain energy, due to the deformation of the solid structure when interacting with the travelling pressure wave. A structure's capability to dissipate acoustic energy is therefore determined by its ability to foster these two energy conversions. A porous structure is particularly indicated for this, since it would allow the penetration of the exterior PW inside its matrix where it would be trapped in a succession of reflections, transferring its energy to the structure in the form of frictional losses and deformations. The morphological characteristics which determine this structure's degree of efficacy are: its pore interconnectivity, the higher the more uniformly the exterior PW is dispersed through the matrix; and its pore size, if too coarse the PW will cross the structure with minimal interaction while if too fine it will not penetrate the surface enough to undergo a substantial level of interactions.

The depositions considered in the following case-studies were based on this insight, corresponding to large porous foams deposited on the plate's chamfer aimed at increasing the system's acoustic damping. Although this was not completely achieved, as exposed on Section 3.1, these foams intended to reconstruct the plates' chamfered-perforations, making its top diameter identical to the bottom one.

Filling with pin vs Filling without pin

The second case-study proposed to investigate the influence of the plate's chamfer filling architecture in the flame's stability. To do so, Sample C was deposited on both plates II and I, but while in the former one the aforementioned pin was placed inside its perforation during the electrodeposition procedure, to delimit the growing foam inner wall geometry and dimensions, in the latter it was not, allowing the deposition to evolve unrestrained during such time.

After this, the chamfer-reconstructed plates' FSDs were measured for the defined resonant duct length and compared to their respective "clean" performance. Results are presented in Figure 11.

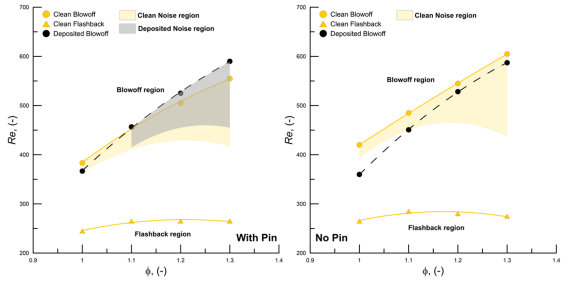

Figure 11: Overlap of plates' II and I stability maps in deposited and non-deposited conditions for $L = 35$ cm. The map on the left evaluates the use of the interior support pin inside plate's II chamfer during its electrodeposition procedure, while the map on the right investigates the absence of such pin during plate's I deposition. The non-deposited plate is associated to yellow symbols while the deposited plate is associated to black symbols. The yellow and grey shaded areas correspond to the non-deposited and deposited plates' self-sustained unstable combustion regions, respectively.

For the plate reconstructed with the use of the interior support pin, the burner does not present significant changes in its stability, exhibiting a blowoff limit and a noise region fairly similar to the ones in its non-deposited condition. However, for the plate reconstructed without the pin, there is a slight decrease in the flame's blowoff limit, particularly for leaner regimes, and a total suppression of the combustion instability region present in its clean condition.

This might indicate that the chamfer filling architecture affects the flame-plate heat balance and relevantly impacts the local thermoviscous effects, consequently changing the burner's acoustic resistance. However, using the Image J software to analyse pictures of the deposition performed without the pin, its bottom diameter was determined equal to 5.28 mm^2 and thus smaller than the one presented by the plate in non-deposited conditions ($d = 6$ mm).

Hence, it is considered more probable that the observed noise extinction was due to a disruption of the flame-burner acoustic coupling mechanism and not due to an increase in the system's acoustic damping. Is is assumed that the exhibited diameter change, albeit the deposition being porous, resulted in a relevant area reduction at the plate's bottom which translated into an increase of the incoming reactant flow's velocity field at the burner's outlet. This led to an increase in the flame's height which significantly changed its dynamics, reducing its blowoff limit and altering its FTF's phase (and possibly its gain), as previously described by [5]. This phase change induced by the variation of the flame's convective time delay, altered the frequency distribution of the flame-generated PW and ended its former overlap with the (unaltered) burner's frequency bandwidth.

Pulsed current filling vs Constant current filling

The final case-study intended to assess the influence of the plate's chamfer filling morphology in the flame's stability. For that, plates' II and I chamfers were deposited with Samples C and D, respectively, both using the support pin inside its perforations during the deposition procedure. As described in Sections 2 and 3.1, Sample C was obtained in a pulsed mode and exhibits no interconnectivity between its pores, while Sample D was produced in a galvanostatic mode and does present interconnectivity between its pores. Moreover, from a qualitative analysis of Figure 6, it is safe to add that the former sample shows a lower mean pore dimension than the latter one; such that Sample C qualitatively presents a lower porosity than Sample D.

Following this, the chamfer-filled plates' FSDs were acquired for the defined resonant duct length and compared to their respective non-deposited behaviour. Results are presented in Figure 12.

For both chamfer-reconstructed plates, their associated blowoff limits remain reasonably identical to the ones exhibited in non-deposited conditions. However, while the plate whose foam presents lower porosity essentially preserves its thermoacoustic instability region size and location, the plate whose foam presents higher porosity exhibits a total suppression of this region.

[2]The Re considered in this chamfer-reconstructed plate FSD was adjusted to take into account this diameter variation.

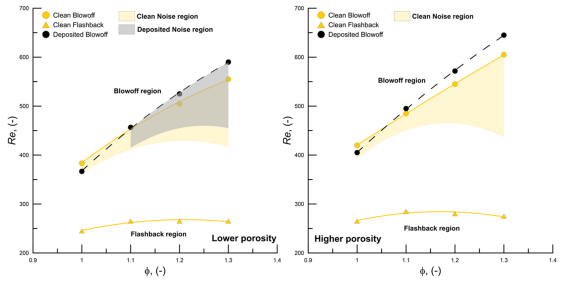

Figure 12: Overlap of plates' II and I stability maps in deposited and non-deposited conditions for $L = 35$ cm. The map on the left analyses the chamfer reconstruction of plate II with a low porosity foam, while the map on the right studies the chamfer reconstruction of plate I with a high porosity foam. The non-deposited plate is associated to yellow symbols while the deposited plate is associated to black symbols. The yellow and grey shaded areas correspond to the non-deposited and deposited plates' self-sustained unstable combustion regions, respectively.

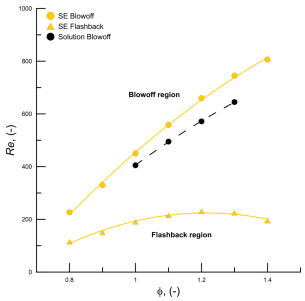

Figure 13: Overlap between the flame stability maps of the SE plate and the high porosity chamfer-reconstructed plate I for $L = 35$ cm. The SE plate is associated to yellow symbols while the deposited plate I is associated to black symbols.

This suggests that the chamfer filling morphology strongly conditions the local thermoviscous effects and consequently the burner's acoustic resistance. Contrarily to the initial illations obtained in the former case-studies, this conclusion is believed to be accurate since it somewhat confirms the findings presented by [14], that a structure's ability to dissipate acoustic energy increases with its pore interconnectivity and with an appropriate tuning of its pore size, and by [5], that the burner's acoustic resistance is mainly conditioned by the thermoviscous effects in the anchoring plate's perforation inner wall boundary layer.

Solution testing

In the third and final case-study, positive results were obtained for $L = 35$ cm, since plate's I chamfer-reconstruction with Sample D was able to completely suppress the self-sustained thermoacoustic instabilities, which naturally arise in its non-deposited condition, by apparently increasing the system's acoustic damping. Hence, a comparison between this new design's stability performance and the more commercially used straight edge perforation design was required.

To do so, the SE plate's FSD was compared with plate's I FSD when chamfer-filled with Sample D, for the defined resonant duct length $L = 35$ cm, in Figure 13.

For the tested equivalence ratios, although both plates present no unstable combustion regions, the SE plate still presents a higher flame stability than the chamfer-reconstructed plate I.

Nonetheless, it should be noted that, as exposed in Section 3.1, the chamfer-reconstruction performed by Sample's D deposition on plate I was not complete (reconstruction proximity = 88.83%), being unable to fill its chamfer to a point where its top diameter coincided with its bottom diameter d. Considering this and the obtained results, it is considered possible that, in case of a complete reconstruction of such chamfer, plate's I blowoff limit would increase to a position substantially closer to the SE plate's blowoff limit.

4. Conclusions

The ultimate goal of this work was to serve as a basis for the creation of an implementable, simple and flexible passive solution which minimizes the development of self-sustained thermoacoustic instabilities in modern open flame multiperforated plate burners. To achieve this, a study was performed in an unconfined single-point injection configuration regarding the influence of specific functional manipulations of the inner wall surface of the anchoring plate's perforation on flame stability. A depiction of the procedure followed in the intended stability analyses was presented, as well as a detailed description of the method used to perform the desired inner wall surface depositions. Before evaluating the flame's stability under different working conditions (Re, ϕ, resonant cavity size, flame anchoring plate, deposition sample), a characterization of the deposition samples was conducted. Results showed the existence of two different compositions: Sample A was essentially composed by Co arrays while Samples B, C and D were mainly composed by a Zn-derived (simonkolleite). Although all samples presented a 3D porous structure typical of foams constructed by the dynamic hydrogen bubble template method, Sample A presented a honeycomb-like structure with relative homogeneity, while Samples B, C and D presented a morphology composed by hexagon-like sub-units, typical of simonkolleite, with only Sample D presenting interconnectivity between its pores. In the stability analysis, an initial characterization of the anchoring plates used

was followed by the presentation of three deposition case-studies, with variations regarding the thermal behaviour of the deposited material, the architecture of its macrostructure and the morphology of its microstructure. The latter analysis provided this work's most relevant conclusions, which are summarized and listed below:

- For the thickness range characteristic of industrial applications of electrodepositions, flame stability in an upward chamfered plate isn't relevantly affected by the chamfer's coating thermal conductivity (λ) or its variation during operation ($\frac{\partial \lambda}{\partial T}$).
- A porous reconstruction of an upward chamfered plate's chamfer, which leads to a decrease in the incoming fresh flow crossing area at the plate's bottom, might translate into a relevant increase of the flame's height and consequently change its dynamics. For a working condition specifically characterized by thermoacoustic instabilities, this change may alter the frequency distribution of the flame-generated PW to a point where its former coupling with the (unaltered) burner's acoustics may cease to exist, stabilizing the combustion process.
- A porous reconstruction of an upward chamfered plate's chamfer, with a high pore interconnectivity level and an appropriately tuned pore size, mitigates the flame's ability to develop self-sustained thermoacoustic instabilities, apparently by increasing the local thermoviscous effects and consequently enhancing the burner's acoustic damping.

Acknowledgements

The author would like to thank Professor Edgar Fernandes and PhD Luísa Marques for all the availability and guidance provided throughout this work.

References

[1] K. R. A. M. Schreel, E. L. van den Tillaart, and L. P. H. De Goey. The influence of burner material properties on the acoustical transfer function of radiant surface burners. *Proceedings of the Combustion Institute*, 30(2):1741–1748, 2005.

[2] T. Schuller, D. Durox, and S. Candel. Self-induced combustion oscillations of laminar premixed flames stabilized on annular burners. *Combustion and Flame*, 135(4):525–537, 2003.

[3] D. Durox, T. Schuller, and S. Candel. Self-induced instability of a premixed jet flame impinging on a plate. *Proceedings of the Combustion Institute*, 29(1):69–75, 2002.

[4] N. Noiray, D. Durox, T. Schuller, and S. Candel. Self-induced instabilities of premixed flames in a multiple injection configuration. *Combustion and Flame*, 145(3):435–446, 2006.

[5] N. Noiray, D. Durox, T. Schuller, and S. Candel. Passive control of combustion instabilities involving premixed flames anchored on perforated plates. *Proceedings of the Combustion Institute*, 31(1):1283–1290, 2007.

[6] M. G. C. Ferreira. Thermoacoustic self-sustained instabilities of conical flames in multi-perforated plate buners. Master's thesis, Instituto Superior Técnico, Universidade de Lisboa, July 2017.

[7] K. R. McManus, T. Poinsot, and S. M. Candel. A review of active control of combustion instabilities. *Progress in Energy and Combustion Science*, 19(1):1–29, 1993.

[8] G. A. Richards, D. L. Straub, and E. H. Robey. Passive control of combustion dynamics in stationary gas turbines. *Journal of Propulsion and Power*, 19(5):795–810, 2003.

[9] W. Qin, C. Yang, X. Ma, and S. Lai. Selective synthesis and characterization of metallic cobalt, cobalt/platinum, and platinum microspheres. *Journal of Alloys and Compounds*, 509(2):338–342, 2011.

[10] L. M. Marques, M. M. Alves, S. Eugénio, S. B. Salazar, N. Pedro, L. Grenho, N. P. Mira, M. H. Fernandes, and M. F. Montemor. Potential anti-cancer and anti-candida activity of zn-derived foams. *Journal of Materials Chemistry B*, 6(18):2821–2830, 2018.

[11] B. J. Plowman, L. A Jones, and S. K. Bhargava. Building with bubbles: the formation of high surface area honeycomb-like films via hydrogen bubble templated electrodeposition. *Chemical Communications*, 51(21):4331–4346, 2015.

[12] P. A. L. F. L. Santos. Stability analysis of premixed laminar propane flames. Master's thesis, Instituto Superior Técnico, Universidade de Lisboa, October 2017.

[13] C. Y. Ho, R. W. Powell, and P. E. Liley. Thermal conductivity of the elements. *Journal of Physical and Chemical Reference Data*, 1(2):279–421, 1972.

[14] M. A. Kuczmarski and J. C. Johnston. Acoustic absorption in porous materials. 2011.